Polymer–inorganic solid–electrolyte interphase for stable lithium metal batteries under lean electrolyte conditions

Yue Gao [1], Zhifei Yan[1], Jennifer L. Gray[2], Xin He[3], Daiwei Wang[4], Tianhang Chen[4], Qingquan Huang[4], Yuguang C. Li[1], Haiying Wang[2], Seong H. Kim [3], Thomas E. Mallouk[1] and Donghai Wang [4]*

The solid–electrolyte interphase (SEI) is pivotal in stabilizing lithium metal anodes for rechargeable batteries. However, the SEI is constantly reforming and consuming electrolyte with cycling. The rational design of a stable SEI is plagued by the failure to control its structure and stability. Here we report a molecular-level SEI design using a reactive polymer composite, which effectively suppresses electrolyte consumption in the formation and maintenance of the SEI. The SEI layer consists of a polymeric lithium salt, lithium fluoride nanoparticles and graphene oxide sheets, as evidenced by cryo-transmission electron microscopy, atomic force microscopy and surface-sensitive spectroscopies. This structure is different from that of a conventional electrolyte-derived SEI and has excellent passivation properties, homogeneity and mechanical strength. The use of the polymer–inorganic SEI enables high-efficiency Li deposition and stable cycling of 4 V Li|LiNi$_{0.5}$Co$_{0.2}$Mn$_{0.3}$O$_2$ cells under lean electrolyte, limited Li excess and high capacity conditions. The same approach was also applied to design stable SEI layers for sodium and zinc anodes.

Rechargeable battery technology based on lithium (Li) metal anodes shows great promise in meeting the energy density demand for portable electronics and electric vehicles[1–4]. In Li metal batteries, the solid–electrolyte interphase (SEI) is crucial in stabilizing the Li anode, both in terms of avoiding undesirable reactions with the electrolyte and in facilitating stable Li deposition. The SEI is a salt layer on the Li surface that is formed by electrolyte decomposition at low operating potentials[5,6]. Unfortunately, the SEI is mechanically unstable under the huge interfacial fluctuations and morphological changes of the Li anode and therefore constantly reforms on cycling[7–9]. This process consumes the electrolyte, resulting in a low efficiency of Li deposition[8,10] and rapid battery failure (Fig. 1a). In this process, the SEI layer becomes progressively structurally inhomogeneous[11], promoting uneven Li deposition and dendrite growth. Although the use of hosts[12–15] and mechanically robust films[16,17] can prevent dendrite growth, the SEI remains unstable, and this has become the bottleneck in Li anode technology.

Researchers have for decades approached this problem in two ways. A routine strategy is to replace the electrolyte-derived SEI by ex-situ-fabricated protective layers such as inorganic salts[18–21], Li alloys[22] and polymers[23–25]. These layers can crack and are not reformable on cycling, triggering Li–electrolyte reactions at the exposed surface. Another approach is to design new electrolytes (for example, concentrated electrolytes[26,27], ionic liquids[28,29] and fluorinated electrolytes[30]) or to use sacrificial additives with conventional electrolytes[31–38]. The so-formed SEI can reduce Li consumption but is nevertheless constantly consuming electrolyte. Consequently, current methods have, in general, achieved cycling stability with a large excess of electrolyte (the electrolyte-to-capacity ratio is typically above 40 µl mAh^{-1}), which lowers the energy density of the battery.

In practical batteries, the mass and volume of electrolyte must be kept below 10 µl mAh^{-1} to achieve high energy density. This requires not only a highly stable SEI layer but also strict prevention of electrolyte loss. Unfortunately, the structure and stability of the electrolyte-derived SEI are determined by the electrolyte, and involve competitive reactions of different solvents and salts. The reaction products deposit onto the Li surface in a spontaneous manner, resulting in a failure to control the composition and structure of the SEI[5,39,40]. An approach to rationally design a stable SEI using a functional SEI precursor rather than the electrolyte is thus needed to address the problem of the unstable SEI and to enable practical Li anodes.

Towards this end, we report here the design of a Li anode SEI using a reactive polymer composite (RPC) as the SEI precursor, namely a poly(vinylsulfonyl fluoride-*ran*-2-vinyl-1,3-dioxolane) (P(SF-DOL))–graphene oxide (GO) nanosheet composite. The SEI consists primarily of polymeric Li salts embedded with nanoparticles of LiF and GO nanosheets (Fig. 1b). This lamellar composite provides excellent SEI stability and effective retention of electrolyte on cycling. The polymer–nanoparticle composite is dense and provides good passivation properties; the on-site formation process ensures homogeneity; and the GO nanosheets confer mechanical strength and help prevent Li dendrite growth. These properties were verified by interfacial studies including cryogenic transmission electron microscopy (cryo-TEM), X-ray photoelectron spectroscopy (XPS) and atomic force microscopy (AFM). The use of the RPC-derived SEI enables dendrite-free Li deposition with a high efficiency (99.1%) at a deposition amount of 4.0 mAh cm^{-2}. Stable cycling (over 200 cycles) of a 4 V Li|LiNi$_{0.5}$Co$_{0.2}$Mn$_{0.3}$O$_2$ (NCM 523) battery cell was achieved under lean electrolyte (7 µl mAh^{-1}), limited Li excess (1.9-fold excess of Li) and high areal capacity

[1]Department of Chemistry, The Pennsylvania State University, University Park, PA, USA. [2]Materials Research Institute, The Pennsylvania State University, University Park, PA, USA. [3]Department of Chemical Engineering and Materials Research Institute, The Pennsylvania State University, University Park, PA, USA. [4]Department of Mechanical and Nuclear Engineering, The Pennsylvania State University, University Park, PA, USA. *e-mail: dwang@psu.edu
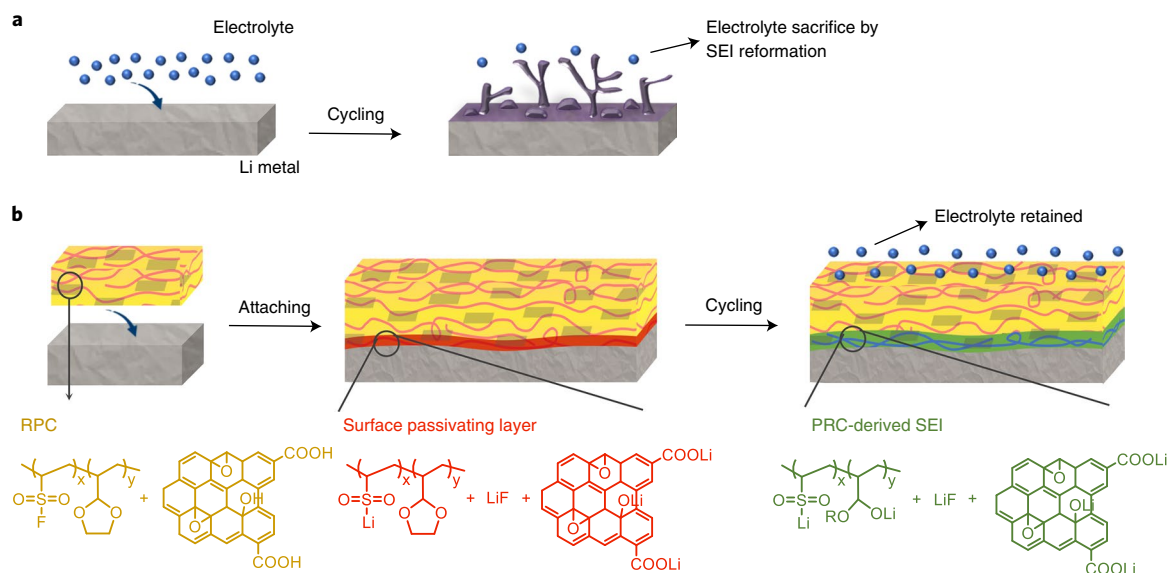
Fig. 1 | Illustration of the molecular-level design of a polymer–inorganic SEI using a reactive polymer composite. a, Formation of an electrolyte-derived SEI via electrolyte decomposition. The SEI layer (purple) is constantly breaking and consuming electrolyte on cycling. **b**, Design of a polymer–inorganic SEI using the RPC precursor rather than the electrolyte. The RPC layer first passivates the Li surface by a chemical reaction. The products form a dense layer (red) that blocks electrolyte access to the surface. The attached RPC subsequently generates polymeric salts and nanoparticles of Li salts on-site. GO nanosheets complete the SEI layer (green). The unreacted RPC (yellow) acts as a reservoir to maintain the SEI structure on cycling.

$(3.4\,mAh\,cm^{-2})$ conditions. Quantitative nuclear magnetic resonance (qNMR) shows that electrolyte reactivity is primarily responsible for the rapid failure of conventional Li|NCM 523 cells. In contrast, the electrolyte is well retained in cells with the RPC-derived SEI. The successful demonstration of high-performance Li metal batteries under lean electrolyte conditions offers promise for the practical use of this approach. This SEI design was also applied to sodium and zinc anodes.

Design of a polymer–inorganic SEI layer

The key to achieving a stable polymer–inorganic SEI is to control the structure and reactivity of the RPC. We screened a variety of organic, inorganic and two-dimensional (2D) compounds to constitute the RPC (Supplementary Figs. 1–5). We found that a combination of a P(SF-DOL) polymer and GO nanosheets provided optimal stabilization for Li anodes (Supplementary Figs. 6–9).

The RPC-derived SEI was formed by a two-step reaction on the Li surface. First, the RPC layer, attached to the Li surface, occupies surface sites via a chemical reaction between Li and sulfonyl fluoride, a fluorinating group. We found LiF and $-SO_2-Li$ salts at the interface, and the COOH groups in the GO were converted to $-CO_2-Li$ (Supplementary Figs. 10 and 11). The formed layer (surface passivating layer in Fig. 1b), containing polymers, nanoscale salt particles and GO nanosheets, is sufficiently dense and blocks electrolyte access to the Li surface (Supplementary Fig. 12). The attached RPC reacts at the interface to form the nanoscale SEI components. This reaction results in an interface that is electrochemically different from that of an electrolyte-derived SEI. This was evidenced by peak shifting in cyclic voltammetry (Supplementary Fig. 13). The unreacted RPC layer on the top of the SEI serves as a reservoir to maintain the SEI on cycling.

To identify the chemistry at the interface, we performed high-resolution XPS, Fourier transform infrared spectroscopy and elemental concentration analyses on the cycled Li after 30 cycles. As schematically illustrated in Fig. 2a, the top surface of the electrode is covered by the unreacted RPC, and the SEI resides in between this unreacted RPC and Li. Figure 2b shows high-resolution XPS spectra of the unreacted RPC. $-SO_2-F$ groups (688.3, 169.4 and

170.6 eV in the F 1s and S 2p spectra, respectively), C–O–C/C–S bonds (286.2 eV in the C 1s spectrum) and $-CO_2-$ groups from GO (289.8 eV in the C 1s spectrum) were observed. These peaks are consistent with those of the pristine RPC (Supplementary Fig. 5d), indicating that the chemical structure of the unreacted RPC remains unaltered.

At the interface, a highly polymeric SEI was detected (Fig. 2c). A detailed peak interpretation is as follows: peaks at 688.5 and 684.5 eV in the F 1s spectrum are attributed to $-SO_2-F$ and LiF, respectively; peaks at 289.9, 288.4, 285.9 and 284.6 eV in the C 1s spectrum belong to $-CO_2-$ from GO, $-CO_2-Li$ from reduced GO and the carbonate electrolyte, C–O and C–S bonds (overlapped) from reduced DOL and $-SO_2-$ groups and C–C bonds from the polymer backbone, respectively; split peaks at 170.2 and 169.0 eV in the S 2p spectrum are assigned to overlapped $-SO_2-F$ and $-SO_2-Li$ groups[41]; peaks at 57.6 and 55.6 eV in the Li 1s spectrum are assigned to Li–F and $-SO_2-Li/-C-O-Li$, respectively. Collectively, the RPC-derived SEI contains a polymer integrating side groups of $-SO_2-Li$ and $-C-O-Li$, LiF nanoparticles and GO nanosheets. From these data, it is clear that the composition of the RPC-derived SEI is distinct from that of a conventional electrolyte-derived SEI, which consists primarily of inorganic Li salts such as Li_2CO_3, $Li_xPO_yF_z$ and Li_2O (Supplementary Fig. 14) and is predominantly inorganic. XPS elemental concentration analysis further supports this finding. The RPC-derived SEI has a high content of C (37.8%) and O (26.3%) and a low content of Li (19.6%) and F (11.2%) (Fig. 2d and Supplementary Fig. 15). This is in clear contrast with the electrolyte-derived SEI, which has high concentrations of Li (37.3%) and F (33.6%) (Fig. 2d). A similar conclusion can be reached from the Fourier transform infrared data (Supplementary Fig. 16).

Polymer–inorganic composite structure of the SEI

After identifying the composition of the RPC-derived SEI, we studied its morphology and nanostructure. The RPC-stabilized Li electrode after 30 cycles has a flat surface morphology, as observed in top- and side-view scanning electron microscopy (SEM) images (Fig. 3a,b and Supplementary Figs. 17 and 18). The optical profilometry image depicts a defect-free surface with small height
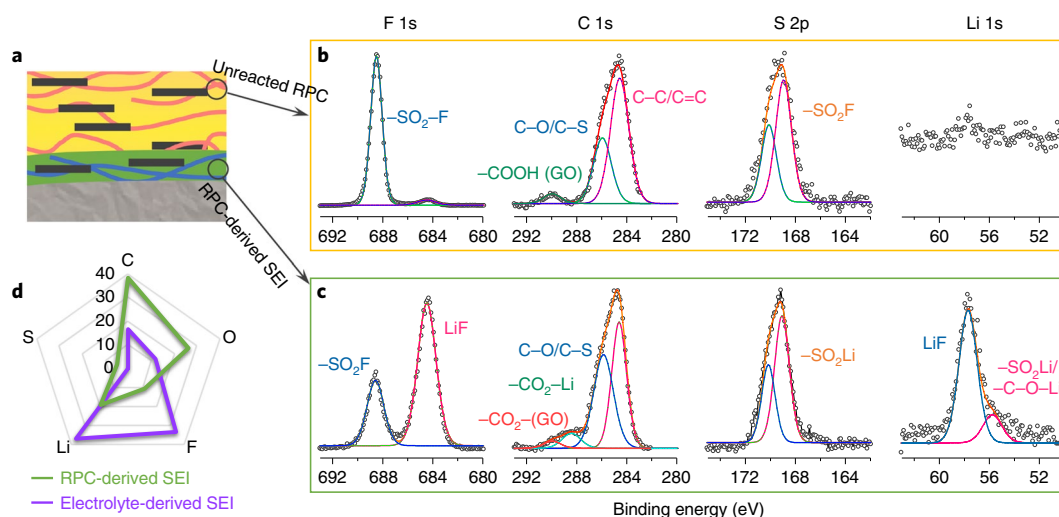
Fig. 2 | SEI chemistry ruled by the RPC rather than the electrolyte. a, Illustration of the cycled RPC-stabilized Li. The electrode surface is covered by an unreacted RPC layer (yellow), and the RPC-derived SEI layer (green) lies in between the unreacted RPC and Li. The black lines represent the GO nanosheets. **b,c**, High-resolution XPS spectra of the unreacted RPC (**b**) and RPC-derived SEI (**c**) layers. The unreacted RPC retains its chemical structure, and the SEI consists primarily of a polymer integrating side groups of –SO_2–Li and –C–O–Li, nanoparticles of LiF and GO nanosheets. **d**, Comparison of the elemental concentrations of the RPC-derived SEI and carbonate electrolyte-derived SEI. The RPC-derived SEI containing high concentrations of C and O is predominantly organic, compared to the electrolyte-derived SEI that contains high concentrations of Li and F.

differences up to 0.8 μm (Fig. 3c). In contrast, the surface of cycled bare Li is very rough (Fig. 3d,e) with height differences up to 7.2 μm (Fig. 3f). Photographs of Li electrodes show that the surface of the RPC-stabilized Li remains shiny, whereas the bare Li surface turns black (Supplementary Fig. 19). The morphology and structure of RPC-stabilized Li are durable after extensive cycling, evidenced by SEM and XPS (Supplementary Fig. 20). Moreover, after removing the unreacted RPC layer, we found that the deposited Li showed a dendrite-free morphology (Supplementary Fig. 21). These findings verify the improved uniformity of Li deposition with the RPC layer.

We next probed the nanostructure of the RPC-derived SEI using cryo-TEM. Figure 3g shows a TEM image of the interface. We observed three layers displaying different contrast, which can be recognized as the unreacted RPC, RPC-derived SEI and Li (from the top to the bottom in Fig. 3g), respectively. The SEI has a thickness of about 90–120 nm and lies in between the unreacted RPC and Li layers. We next captured high-resolution images in the squared regions to study the specific nanostructure of these three layers. In the Li layer (Fig. 3h, the squared region in purple), we observed the {110} Li plane with a lattice spacing of 0.25 nm, consistent with deposited Li[42–44]. The lattice spacing was confirmed in a corresponding fast Fourier transform image (Supplementary Fig. 22c,d). In the RPC-derived SEI layer (Fig. 5i, the squared region in red), we saw an amorphous layer containing embedded nanocrystals. The lattice spacings of these nanocrystals are 0.20 and 0.23 nm, corresponding to the {200} and {111} LiF planes, respectively (Supplementary Fig. 22a,b). The majority of the SEI is amorphous and can be identified as polymeric Li salts. Another RPC component, the GO nanosheets, shows a wavy morphology in both the unreacted RPC and the SEI layers (Supplementary Figs. 23 and 24). Encouragingly, unlike a conventional electrolyte-derived SEI that shows multiple-layered[42] or porous[44] nanostructures, the RPC-derived SEI is homogeneous and dense. This is the key reason for the improved SEI stability and effective suppression of dendritic Li growth. It is also worth noting that the characteristic components derived from electrolyte decomposition such as Li_2CO_3 crystals were not found in the TEM image (Fig. 3i) of the RPC-derived SEI. This finding is consistent with the result of XPS studies that the concentration of

the electrolyte-derived –CO_2–Li (the peak at 289.1 eV in the C 1s spectrum) was very limited.

We further elucidated the interfacial chemical compositions using electron energy-loss spectroscopy (EELS) and energy-dispersive X-ray spectroscopy (EDS). Figure 3j shows a scanning transmission electron microscopy (STEM) image of the cycled RPC-stabilized Li. We boxed a region containing the unreacted RPC, SEI and Li layers and analysed the composition pixel-by-pixel (Fig. 3k). The Li K-edge spectrum taken from the bottom purple area shows a broad peak centred at 63 eV, corresponding to Li metal. The peak shape in the red area spectrum corresponds to LiF, indicating that this area belongs to the SEI. We observed a very low Li intensity in the green top region and thus identified it as the unreacted RPC layer. The presence of the weak Li signal is probably caused by beam-induced diffusion of Li. In the EDS image based on the STEM image, we also identified the three different layers (Fig. 3l). The top layer containing S, F and C was assigned to the unreacted RPC. The middle layer showing S and F was identified as the SEI. The bottom layer shows very weak C, F and S signals, which can be attributed to Li. XPS depth profiling further confirms the three-layer structure (Supplementary Fig. 25). Taken together, these data clearly show that the RPC-derived SEI is primarily composed of polymeric Li salts, embedded nanoparticles of LiF and GO nanosheets, giving it excellent homogeneity and density.

We also investigated the changes in chemical and physical properties of the SEI layer due to the addition of GO nanosheets. The mechanical strength of the RPC-derived SEI layer was measured using AFM indentation (Supplementary Figs. 26 and 27). The presence of GO nanosheets in the SEI enables it to have both good modulus and flexibility, which are normally mutually exclusive. The improved mechanical strength ensures that the SEI has good tolerance to the interfacial fluctuations that occur during Li deposition. Note that the use of GO nanosheets can also prevent dendrite growth[45] (Supplementary Figs. 28 and 29).

Stable interface of RPC-stabilized Li anodes
To examine the interfacial stability of Li anodes on cycling, we conducted a plating/stripping test for Li anodes with and without the RPC. RPC-stabilized Li displays stable resistance (Fig. 4a
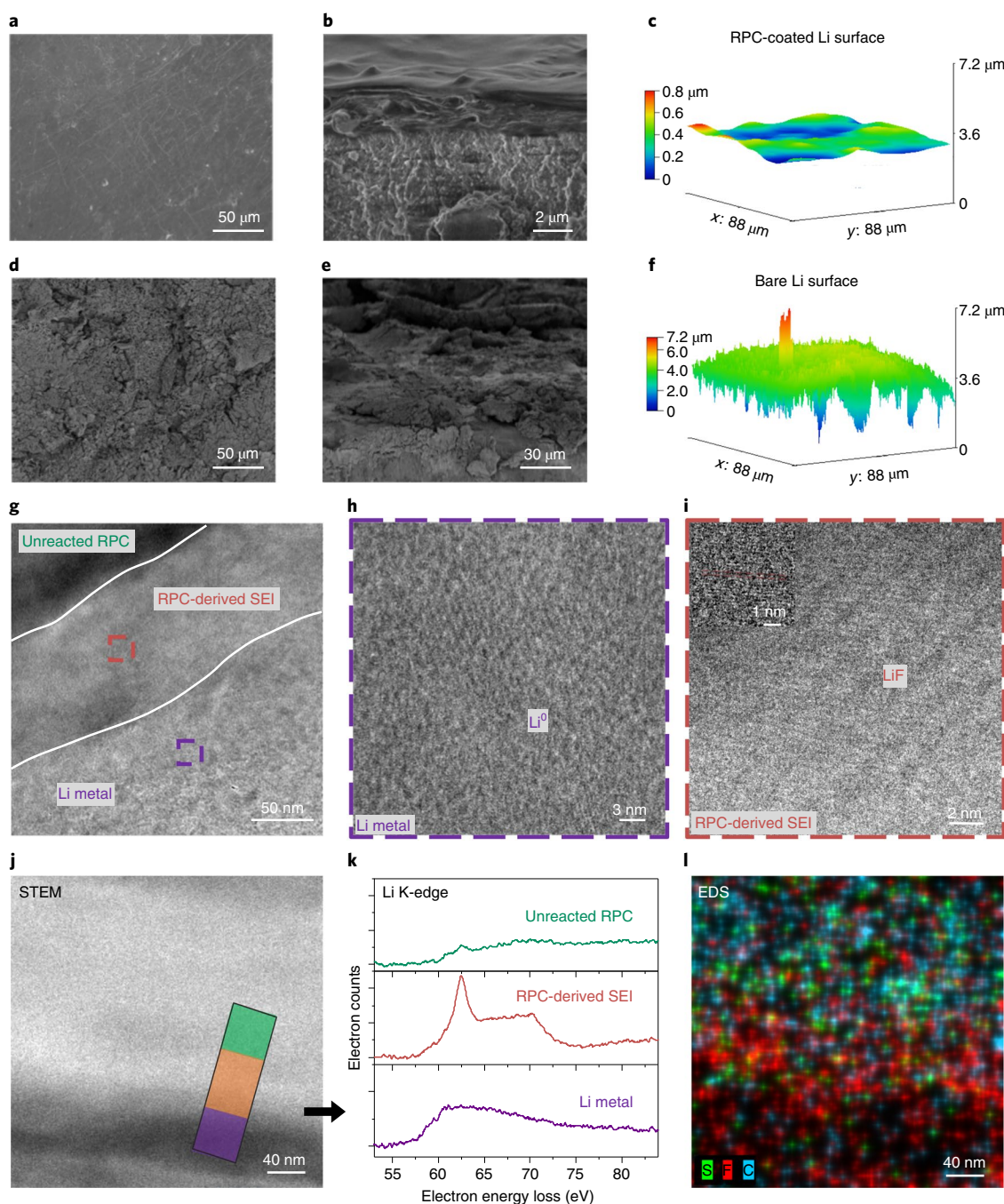
Fig. 3 | Polymer–inorganic composite structure of the RPC-derived SEI. a–c, Morphology of the cycled RPC-stabilized Li, observed by top-view (**a**) and side-view (**b**) SEM and optical profilometry images of the surface (**c**). **d–f**, Morphology of the cycled bare Li, probed by top-view (**d**) and side-view (**e**) SEM and optical profilometry images (**f**). **g–i**, TEM images of the interface of RPC-stabilized Li. Three layers were found at the interface (**g**), recognized as the unreacted RPC, RPC-derived SEI and Li, respectively. In the Li region (**h**), metallic Li lattices were observed. In the RPC-derived SEI layer (**i**), we saw an amorphous layer containing embedded LiF nanocrystals. **j**, STEM image of the interface of the RPC-stabilized Li. **k**, Li K-edge spectra of the boxed regions in **j**. **l**, EDS image based on **j**. A three-layer structure at the interface was confirmed. All of the RPC-stabilized Li samples were collected after 30 cycles.

and Supplementary Fig. 30) and voltage profiles (Supplementary Figs. 31 and 32), while those of bare Li increase dramatically (Fig. 4b and Supplementary Fig. 31). The use of the RPC with an optimal thickness of 3 μm gives a moderate Li deposition overpotential (Supplementary Fig. 33). The efficiency of Li deposition at a high Li deposition amount of 4.0 mAh cm^{-2} was measured in a Li|3D host cell. The use of 3D hosts reduces interfacial fluctuations during Li deposition (Supplementary Fig. 34). An average efficiency

of 99.1% was achieved in 300 cycles at a current density of 2.0 mA cm^{-2} (Fig. 4c). Moreover, when we increased the deposition amount to 8.0 mAh cm^{-2}, Li deposition remains stable and exhibits a high average efficiency of 98.6% (Supplementary Fig. 35a,b). An average efficiency of 99.3% was attained when flat stainless-steel foils were used as the current collector (Supplementary Fig. 35c). In addition, we used the RPC to construct stable SEI layers for sodium (Na) and zinc (Zn) battery anodes. High efficiencies and extended
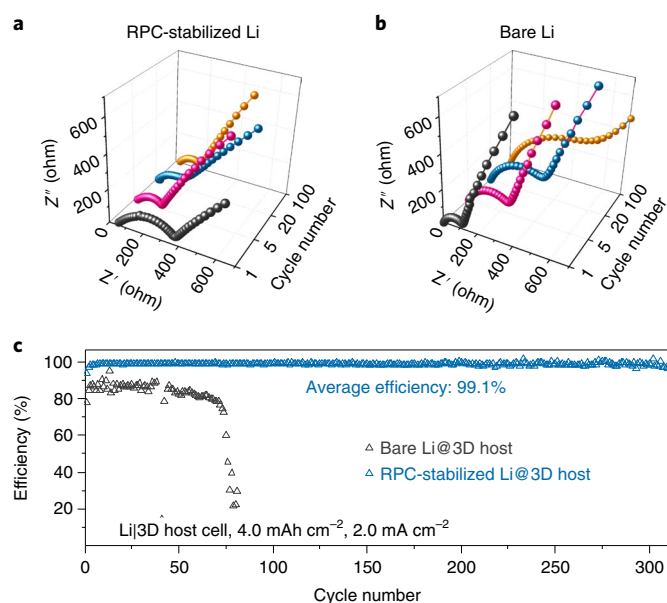
Fig. 4 | Interfacial stability of RPC-stabilized Li anodes. a,b, Electrochemical impedance spectroscopy measurements of symmetric cells using RPC-stabilized (**a**) and bare (**b**) Li. **c**, Efficiency of Li deposition in Li|3D host cells at a capacity of 4.0 mAh cm^{-2}.

lifespans were realized for both Na and Zn deposition in metal|3D host cells, respectively (Supplementary Fig. 36).

Li metal batteries under lean electrolyte conditions

To demonstrate the SEI stability, we cycled Li metal batteries under lean electrolyte conditions. NCM 523 was used as the cathode material and pre-delithiated to pair with Li anodes. We initially ran the cell under lean electrolyte (12 μl mAh^{-1}) and excess Li (400 μm Li foil) conditions. A cell incorporating the RPC-derived SEI had a capacity retention of 77.1% in 600 cycles (Supplementary Fig. 37). Even when less Li was used as the anode (120 μm Li foil), the cells surprisingly showed similar lifespans (Fig. 5a and Supplementary Fig. 38). In contrast, the capacity of the control cell faded rapidly after 40 cycles. These results verify that the stable interface and restrained electrolyte loss decisively determine the cycling stability of Li metal batteries under lean electrolyte conditions.

Following these experiments, we used more practical conditions to test the cells. The electrolyte-to-capacity ratio was reduced to 7 μl mAh^{-1}; 1.9-fold excess of Li in a 3D host, and the cell capacity was elevated to 3.4 mAh cm^{-2}. The Li|NCM 523 cell incorporating the RPC-derived SEI displays a capacity retention of 90.7% (Fig. 5b) and stable voltage profiles after 200 cycles (Supplementary Fig. 39), whereas the capacity of the control cell has a cliff-style drop after only 14 cycles, resulting from the severe electrolyte decomposition (Fig. 5b). Changes in the amount of electrolyte remaining on cycling were monitored by tracking the quantity of hexafluorophosphate (PF$_6$) anions in the cell using ^{19}F qNMR, since F signals come exclusively from the LiPF$_6$ salt in the conventional electrolyte. The amount of electrolyte before cycling was normalized to 100% by comparing the peak area of PF$_6$ anions (-71.8 and -73.3 ppm in ^{19}F NMR spectra) with a known amount of an internal reference (fluorobenzene, -113.2 ppm in the ^{19}F NMR spectra). In the control cell, the electrolyte amount decreased to 41% after 50 cycles (Fig. 5c), and the cell could not be cycled. When fresh electrolyte was added, we found that 53% of the Li was still retained in the cell (Supplementary Fig. 40). In the cell incorporating the RPC-derived SEI, we recorded an electrolyte retention of 77% after 180 cycles (Fig. 5d), and 57% of the Li was left (Supplementary Fig. 41). On the basis of these results,
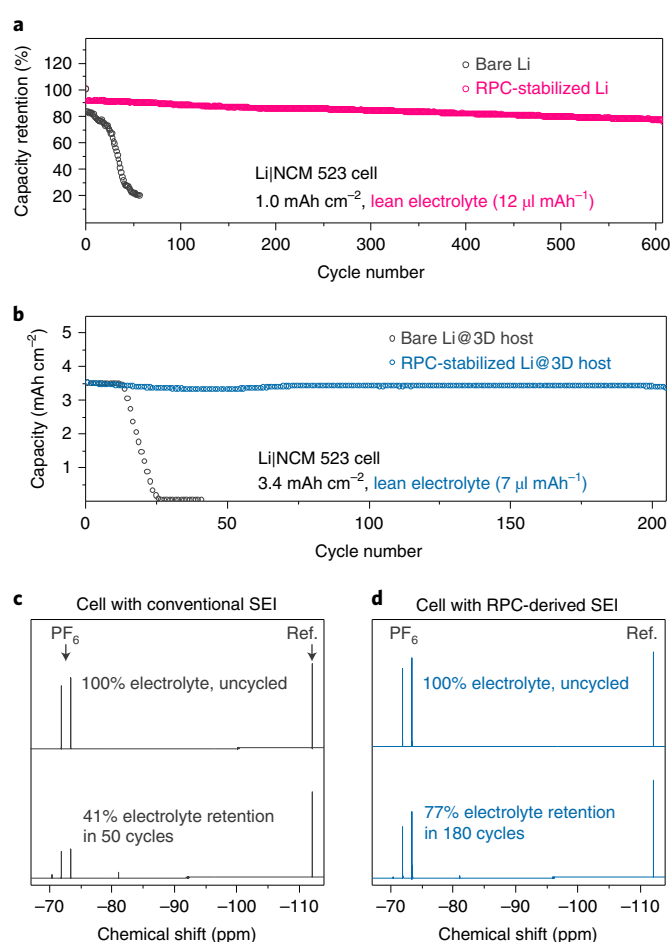
Fig. 5 | Electrochemical performance of Li|NCM 523 batteries under lean electrolyte conditions. a, Cycling stability of Li|NCM 523 cells tested under lean electrolyte (12 μl mAh^{-1}) and excess Li (120 μm Li foil) conditions. **b**, Cycling stability of Li|NCM 523 cells tested under lean electrolyte (7 μl mAh^{-1}), limited Li excess (1.9-fold excess of Li in a 3D host) and high capacity (3.4 mAh cm^{-2}) conditions. **c,d**, ^{19}F NMR spectra of the electrolyte taken from cells with electrolyte-derived SEI (**c**) and RPC-derived SEI (**d**), respectively. The initial electrolyte amount correlating with the area of PF$_6$ before cycling was normalized to 100%. Fluorobenzene (ref.) was used as the internal reference.

we concluded that the polymer–inorganic structure of the RPC-derived SEI confers good stability and effective suppression of electrolyte decomposition, which enables stable cycling of the Li metal batteries under lean electrolyte conditions. This is a step forward in reducing the excessive usage of electrolyte in the Li metal batteries (Supplementary Table 1). In addition, the RPC-derived SEI is stable at an elevated temperature of 45 °C, enabling stable cycling of Li|NCM 523 cells (Supplementary Fig. 42).

Conclusions

In summary, we have demonstrated a new approach to design a polymer–inorganic SEI for Li anodes using a reactive polymeric composite rather than a reactive electrolyte. The so-formed SEI has excellent passivation, homogeneity and mechanical strength, and thus effectively stabilizes the Li/electrolyte interface and prevents electrolyte decomposition on cycling. Apart from realizing highly efficient Li deposition, the use of RPC-derived SEI enables stable cycling of Li metal batteries under lean electrolyte, limited Li excess and high capacity conditions. This approach is also applicable to SEI design for Na and Zn metal anodes.

Online content

Any methods, additional references, Nature Research reporting summaries, source data, statements of data availability and associated accession codes are available at https://doi.org/10.1038/s41563-019-0305-8.

References

1. Tarascon, J. M. & Armand, M. Issues and challenges facing rechargeable lithium batteries. *Nature* **414**, 359–367 (2001).
2. Goodenough, J. B. & Park, K.-S. S. The Li-ion rechargeable battery: a perspective. *J. Am. Chem. Soc.* **135**, 1167–1176 (2013).
3. Choi, N. S. et al. Challenges facing lithium batteries and electrical double-layer capacitors. *Angew. Chem. Int. Ed.* **51**, 9994–10024 (2012).
4. Kim, H. et al. Metallic anodes for next generation secondary batteries. *Chem. Soc. Rev.* **42**, 9011–9034 (2013).
5. Peled, E. & Menkin, S. Review—SEI: past, present and future. *J. Electrochem. Soc.* **164**, A1703–A1719 (2017).
6. Aurbach, D. Review of selected electrode-solution interactions which determine the performance of Li and Li ion batteries. *J. Power Sources* **89**, 206–218 (2000).
7. Lin, D., Liu, Y. & Cui, Y. Reviving the lithium metal anode for high-energy batteries. *Nat. Nanotechnol.* **12**, 194–206 (2017).
8. Xu, W. et al. Lithium metal anodes for rechargeable batteries. *Energy Environ. Sci.* **7**, 513–537 (2014).
9. Cheng, X. B., Zhang, R., Zhao, C. Z. & Zhang, Q. Toward safe lithium metal anode in rechargeable batteries: a review. *Chem. Rev.* **117**, 10403–10473 (2017).
10. Tikekar, M. D., Choudhury, S., Tu, Z. & Archer, L. A. Design principles for electrolytes and interfaces for stable lithium-metal batteries. *Nat. Energy* **1**, 16114 (2016).
11. Sacci, R. L. et al. Direct visualization of initial SEI morphology and growth kinetics during lithium deposition by in situ electrochemical transmission electron microscopy. *Chem. Commun.* **50**, 2104 (2014).
12. Lin, D. et al. Layered reduced graphene oxide with nanoscale interlayer gaps as a stable host for lithium metal anodes. *Nat. Nanotechnol.* **11**, 626–632 (2016).
13. Ye, H. et al. Stable Li plating/stripping electrochemistry realized by a hybrid Li reservoir in spherical carbon granules with 3D conducting skeletons. *J. Am. Chem. Soc.* **139**, 5916–5922 (2017).
14. Yan, K. et al. Selective deposition and stable encapsulation of lithium through heterogeneous seeded growth. *Nat. Energy* **1**, 16010 (2016).
15. Li, G. et al. Stable metal battery anodes enabled by polyethylenimine sponge hosts by way of electrokinetic effects. *Nat. Energy* **3**, 1076–1083 (2018).
16. Tung, S.-O., Ho, S., Yang, M., Zhang, R. & Kotov, N. A. A dendrite-suppressing composite ion conductor from aramid nanofibres. *Nat. Commun.* **6**, 6152 (2015).
17. Cheng, X.-B. et al. Nanodiamonds suppress the growth of lithium dendrites. *Nat. Commun.* **8**, 336 (2017).
18. Li, N.-W., Yin, Y.-X., Yang, C.-P. & Guo, Y.-G. An artificial solid electrolyte interphase layer for stable lithium metal anodes. *Adv. Mater.* **28**, 1853–1858 (2016).
19. Dudney, N. J. Addition of a thin-film inorganic solid electrolyte (Lipon) as a protective film in lithium batteries with a liquid electrolyte. *J. Power Sources* **89**, 176–179 (2000).
20. Kazyak, E., Wood, K. N. & Dasgupta, N. P. Improved cycle life and stability of lithium metal anodes through ultrathin atomic layer deposition surface treatments. *Chem. Mater.* **27**, 6457–6462 (2015).
21. Zhao, J. et al. Surface fluorination of reactive battery anode materials for enhanced stability. *J. Am. Chem. Soc.* **139**, 11550–11558 (2017).
22. Liang, X. et al. A facile surface chemistry route to a stabilized lithium metal anode. *Nat. Energy* **6**, 17119 (2017).
23. Tu, Z. et al. Designing artificial solid–electrolyte interphases for single-ion and high-efficiency transport in batteries. *Joule* **1**, 394–406 (2017).
24. Liu, K. et al. Lithium metal anodes with an adaptive "Solid–liquid" interfacial protective layer. *J. Am. Chem. Soc.* **139**, 4815–4820 (2017).
25. Choi, S. M. et al. Cycling characteristics of lithium metal batteries assembled with a surface modified lithium electrode. *J. Power Sources* **244**, 363–368 (2013).
26. Qian, J. et al. High rate and stable cycling of lithium metal anode. *Nat. Commun.* **6**, 6362 (2015).
27. Suo, L., Hu, Y.-S., Li, H., Armand, M. & Chen, L. A new class of solvent-in-salt electrolyte for high-energy rechargeable metallic lithium batteries. *Nat. Commun.* **4**, 1481 (2013).
28. Basile, A., Bhatt, A. I. & O'Mullane, A. P. Stabilizing lithium metal using ionic liquids for long-lived batteries. *Nat. Commun.* **7**, ncomms11794 (2016).
29. Lu, Y., Korf, K., Kambe, Y., Tu, Z. & Archer, L. A. Ionic–liquid–nanoparticle hybrid electrolytes: applications in lithium metal batteries. *Angew. Chem. Int. Ed.* **53**, 488–492 (2014).
30. Fan, X. et al. Non-flammable electrolyte enables Li-metal batteries with aggressive cathode chemistries. *Nat. Nanotechnol.* **13**, 715–722 (2018).
31. Zheng, J. et al. Electrolyte additive enabled fast charging and stable cycling lithium metal batteries. *Nat. Energy* **2**, 17012 (2017).
32. Lu, Y., Tu, Z. & Archer, L. A. Stable lithium electrodeposition in liquid and nanoporous solid electrolytes. *Nat. Mater.* **13**, 961–969 (2014).
33. Markevich, E., Salitra, G. & Aurbach, D. Fluoroethylene carbonate as an important component for the formation of an effective solid electrolyte interphase on anodes and cathodes for advanced Li-ion batteries. *ACS Energy Lett.* **2**, 1337–1345 (2017).
34. Zhang, Y. et al. Dendrite-free lithium deposition with self-aligned nanorod structure. *Nano Lett.* **14**, 6889–6896 (2014).
35. Chen, S. et al. Functional organosulfide electrolyte promotes an alternate reaction pathway to achieve high performance in lithium-sulfur batteries. *Angew. Chem. Int. Ed.* **55**, 4231–4235 (2016).
36. Ding, F. et al. Dendrite-free lithium deposition via self-healing electrostatic shield mechanism. *J. Am. Chem. Soc.* **135**, 4450–4456 (2013).
37. Li, G. et al. Organosulfide-plasticized solid–electrolyte interphase layer enables stable lithium metal anodes for long-cycle lithium-sulfur batteries. *Nat. Commun.* **8**, 850 (2017).
38. Zhang, H. et al. Electrolyte additives for lithium metal anodes and rechargeable lithium metal batteries: progress and perspectives. *Angew. Chem. Int. Ed.* **57**, 15002–15027 (2018).
39. Aurbach, D., Zinigrad, E., Cohen, Y. & Teller, H. A short review of failure mechanisms of lithium metal and lithiated graphite anodes in liquid electrolyte solutions. *Solid State Ion.* **148**, 405–416 (2002).
40. Gao, Y. et al. Interfacial chemistry regulation via a skin-grafting strategy enables high-performance lithium-metal batteries. *J. Am. Chem. Soc.* **139**, 15288–15291 (2017).
41. Gao, Y. et al. Salt-based organic–inorganic nanocomposites: towards a stable lithium metal/$Li_{10}GeP_2S_{12}$ solid electrolyte interface. *Angew. Chem. Int. Ed.* **57**, 13608–13612 (2018).
42. Li, Y. et al. Atomic structure of sensitive battery materials and interfaces revealed by cryo-electron microscopy. *Science* **358**, 506–510 (2017).
43. Wang, X. et al. New insights on the structure of electrochemically deposited lithium metal and its solid electrolyte interphases via cryogenic TEM. *Nano Lett.* **17**, 7606–7612 (2017).
44. Zachman, M. J., Tu, Z., Choudhury, S., Archer, L. A. & Kourkoutis, L. F. Cryo-STEM mapping of solid–liquid interfaces and dendrites in lithium-metal batteries. *Nature* **560**, 345–349 (2018).
45. Foroozan, T. et al. Synergistic effect of graphene oxide for impeding the dendritic plating of Li. *Adv. Funct. Mater.* **28**, 1705917 (2018).

Author contributions

Y.G., T.E.M. and Do.W. conceived the idea, Y.G. and Do.W. designed the experiments, and Do.W. directed the project. Y.G. performed the material preparation and chemical and morphological characterization. Z.Y. prepared the graphene oxide materials. H.W. prepared the samples for cryo-TEM experiments. J.L.G. performed the cryo-TEM experiments. Y.G. and T.C. performed the battery tests. X.H. conducted the AFM indentation test. Y.G. and Y.C.L. performed the electrochemical impedance spectroscopy test. Y.G. and Da.W. conducted the SEM test. All authors discussed and analysed the data. Y.G., S.H.K, T.E.M. and Do.W. wrote the manuscript.

Competing interests

The authors declare no competing interests.

Additional information

Supplementary information is available for this paper at https://doi.org/10.1038/s41563-019-0305-8.

Reprints and permissions information is available at www.nature.com/reprints.

Correspondence and requests for materials should be addressed to D.W.

Publisher's note: Springer Nature remains neutral with regard to jurisdictional claims in published maps and institutional affiliations.

Methods

Materials. All reagents and solvents were purchased from Sigma-Aldrich and Alfa Aesar and used without further purification unless otherwise stated. The $LiNi_{0.5}Co_{0.2}Mn_{0.3}O_2$ cathode material was supplied by Umicore. Battery-grade lithium hexafluorophosphate ($LiPF_6$), fluoroethylene carbonate (FEC), ethylene carbonate (EC) and ethyl methyl carbonate (EMC) were purchased from BASF. Lithium bis(oxalato)borate (LiBOB) was purchased from Top New Energy Company. Li chips with the thickness of 400 and 120 μm were purchased from MTI.

Preparation of GO solutions. Unilamellar GO solutions were prepared following a modified Hummers method[46]. Pre-oxidation was conducted to ensure complete exfoliation of graphite powder. The graphite powder (3 g) was added to a mixture of concentrated H_2SO_4 (25 ml), $K_2S_2O_8$ (2.5 g) and P_2O_5 (2.5 g) at 80 °C. The mixture was kept at the same temperature for 6 h. The resulting mixture was then carefully diluted with 100 ml distilled water, filtered and washed, followed by drying at 60 °C overnight. The pre-oxidized graphite powder was slowly added to cold (0 °C) concentrated H_2SO_4 (120 ml). $KMnO_4$ (12 g) was added afterward while the temperature of the mixture was kept below 10 °C with an ice bath. The mixture was stirred at 35 °C for 4 h. Distilled water (100 ml) was added and the mixture was stirred at 45 °C for 2 more hours. To terminate the reaction, distilled water (300 ml) and H_2O_2 (6 ml) were added within 15 min, resulting in a bright yellow solution. The mixture was filtered and washed with 1:10 HCl solution to remove additional ions. The GO solution was diluted and subjected to dialysis for one week. Exfoliated GO was prepared by diluting the GO solution to 1 mg ml⁻¹ and sonicating for 15 min. The aqueous solvent of the GO solution was replaced with dimethylformamide by the following method: 90 ml dimethylformamide was added to 10 ml of the as-prepared GO solution (1 mg ml⁻¹). The solution was sonicated and afterward was concentrated to ~10 ml on a rotary evaporator. This process was repeated six times to remove water. Anhydrous sodium sulfate was added to the solution, which was then filtered after 15 min. Anhydrous toluene (90 ml) was then added to the solution, and the solution was concentrated on a rotary evaporator. After repeating this process 6 times, the solution was concentrated to ~2 mg ml⁻¹ on a rotary evaporator.

Preparation of RPC-stabilized metal electrode. Freshly synthesized P(SF-DOL) was added to GO sheets dispersed in anhydrous tetrahydrofuran (THF). The solution was sonicated at 60 °C for 4 h under an argon atmosphere. Li chips were washed with anhydrous hexane three times and dried in a vacuum chamber before use. The solution was coated onto the surface of Li, and the sample was dried in a vacuum chamber for 6 h. To prepare RPC-stabilized Li@3D host electrodes, we electrochemically deposited a certain amount of Li onto the surface of the host (1 cm²) and then vigorously washed the electrode with EMC and hexane many times to remove the SEI layer on it. After drying the electrode, we immersed it into a concentrated RPC solution for 8 h and then dried the electrode in a vacuum chamber. The Na and Zn electrodes were prepared in the same way. All coating procedures were conducted in an argon-filled glovebox.

Characterization. XPS experiments were carried out on a PHI VersaProbe II Scanning XPS Microprobe. Air- and moisture-sensitive samples were loaded in a glovebox and transferred into the instrument through a vacuum transfer vessel. A 20 eV argon ion beam was employed for the XPS depth profiling experiment. ¹H, ⁷Li and ¹⁹F NMR experiments were conducted on a Bruker AV-3-HD-500 instrument. ¹H NMR spectra were calibrated by using residual solvent peaks as the internal reference, and ⁷Li NMR spectra were obtained without internal references. Gel permeation chromatography) tests were conducted on a Hewlett-Packard HP 1100 instrument with a Hewlett-Packard 1047A refractive index detector using two Phenomenex Phenogel linear 10 columns. THF was used for eluting the samples, and elution times were calibrated with a polystyrene standard. Cyclic voltammetry and electrochemical impedance spectroscopy measurements were carried out on a Nuvant EZStat Pro instrument with a three-electrode system. In cyclic voltammetry experiments, bare Cu and RPC-coated Cu foils were employed as a working electrode; respectively, Li foil was used as counter and reference electrodes. Electrochemical impedance spectroscopy measurements for stainless steel|Li cells were conducted between 0.1 and 100,000 Hz with a voltage amplitude of 10 mV. The cells were cycled with 1, 5, 50 and 100 cycles with a Li plating/stripping amount of 1.0 mAh cm⁻². SEM images were captured on a Nova NanoSEM 630 instrument. Profilometry optical images were acquired on a Zygo Nexview 3d Optical Profilometer. The indentation behaviours were tested through an AFM equipped with a Digital Instruments Multimode scanning probe microscope and an environmentally controlled system. Contact angle measurement was performed on aramé-hart Model 295 with an environment control glovebox.

Compositional analysis of the surface passivating layers and SEI layers. To prepare samples for XPS experiments, the cleaned Li chip was contacted with a P(SF-DOL) film (~20 μm) under a pressure of 10 MPa for 12 h. After separating the Li and the polymer films, we immediately conducted an XPS test on the

contact surfaces on the polymer and Li sides, respectively. To prepare the samples for ⁷Li NMR experiments, we added 1.0 g of finely divided Li chips into a THF solution of 0.1 g polymer. After stirring the mixture for 8 h, the solid Li was filtered. The liquid solution was dropped into anhydrous hexane, and a white precipitate appeared, which was the polymeric product from the reaction between the polymer and Li. The precipitate was then dissolved in deuterated dimethylsulfoxide for ⁷Li NMR experiments. A blank THF solution without P(SF-DOL) was used as a control sample, prepared by the same method. All of these procedures were performed in an argon-filled glovebox. The cycled RPC-stabilized and bare Li electrodes were washed with EMC three times, and then dried in a vacuum chamber for XPS and infrared tests. The samples for Na and Zn electrodes were prepared in the same way. All of these procedures were conducted in an argon-filled glovebox.

Cryo-TEM experiment. Cross-sectional TEM samples of the cycled RPC-stabilized Li were prepared on an FEI Helios Nanolab 660 Dual Beam focused ion beam using the 'in situ lift-out' technique. A thin section was extracted from the electrode and attached to a TEM grid using an initial ion beam voltage of 30 kV. The sample was then further thinned using successively lower ion beam voltages until 2 kV, at which point the final thickness was approximately 100 nm. The sample was then quickly transferred to the cryo-TEM holder and inserted into the microscope to minimize exposure to air. TEM and STEM images were captured on a dual spherical aberration-corrected FEI Titan² G2 60-300 STEM at an accelerating voltage of 200 kV. EDS maps were collected in STEM mode using Bruker Super-X quad X-ray detectors, which when combined with a high-brightness X-field emission gun source produce sufficient quality elemental maps within 5 min at a beam current of approximately 0.1 nA. The convergence semi-angle used for STEM imaging was 28.9 mrad. EELS spectral imaging was performed using a Gatan GIF Quantum ERS 966 system. The EELS data were acquired using an exposure time of 0.1 s and a dispersion of 0.05 eV per channel with a pixel size of 10 nm.

AFM indentation experiment. The indentation experiments of the pristine RPC and RPC without GO samples were conducted on the surfaces of the corresponding films (~3 μm), respectively. The indentation experiments of the SEI layers were performed on the cycled Li electrodes after washing with EMC. The thin films (~100 nm) of RPC and P(SF-DOL) were coated on the Li, respectively. The silicon AFM probe was cleaned with ultraviolet/ozone to remove residual chemicals before each test. The Sader method[47] was used to estimate the spring constant of the cantilever. The normal deflection changes of the cantilever during compression and decompression of the SEI surface with the AFM tip were monitored. The cantilever bending was subtracted from the total moving distance of the piezo to obtain only the sample deformation.

The elastic modulus of the RPC-derived SEI was investigated using AFM indentation tests. The Oliver–Pharr model can be used when the surface energy is neglected; here, the stiffness is calculated from the unloading curve. The Poisson ratio of the surfaces was roughly estimated as 0.4, which can be found in some studies[48,49]. Alternatively, the Derjaguin–Muller–Toporov (DMT) contact mechanical model can also be employed to determine the elastic modulus of surfaces taking into account surface energy. The DMT equation is derived as given below.

To simplify the fitting equation, the contact radius a and normal load F are expressed as the following non-dimensional relationship[50,51]:

$$\frac{a}{a_0} = \left(1 - \frac{F}{F_{adh}}\right)^{\frac{1}{3}} \tag{1}$$

where a_0 is the contact radius at zero load, and F_{adh} is the 'pull-off force' in the AFM force–distance curve. The pull-off force is given by the DMT theory as:

$$F_{adh} = 2\pi\gamma R \tag{2}$$

where γ is the interfacial energy and R is the curvature radius of the contact asperity (AFM tip).

The relationship between sample deformation d and normal load F (which is obtained from the force–distance curve) can be obtained by substituting equation (1) into:

$$d = \frac{a^2}{R} \tag{3}$$

yielding the following equation for fitting:

$$d - d_{contact} = \frac{a_0^2}{R}\left(1 - \frac{F}{F_{adh}}\right)^{\frac{2}{3}} \tag{4}$$

where $d_{contact}$ represents the apparent displacement at which the tip first contacts the surface[52]. From the fitting parameters, the reduced elastic modulus can be calculated by:

$$E_r = \frac{3RF_{adh}}{4a_0^3} \tag{5}$$

Electrochemical testing. Electrochemical tests of cells were carried out on Landt battery testers using CR2016 coin cells under galvanostatic charging–discharging conditions at different currents. To prepare the samples for the cyclic voltammetry test, a thin RPC film (~200 nm) coated onto a Cu foil was used as the working electrode. Li chips were used as counter and reference electrodes. The scan rate was 10 mV s^{-1}, and the electrode area was ~2 cm^2. Bare Cu foil was used as the working electrode for the control sample. LiPF$_6$ (1 M) in EC/EMC/FEC (3:7:1, v/v/v) electrolyte was used for the symmetric Li cell test, cyclic voltammetry experiment and the preparation of the cycled RPC-stabilized Li and bare Li samples for characterization. An FEC-free electrolyte (1 M LiPF$_6$ in EC/EMC with 2% LiBOB) was used for measuring the efficiency of metal deposition and evaluating the cycling stability of Li metal battery cells. To measure the efficiency, we pre-plated 4.0 mAh cm^{-2} Li onto the carbon-based 3D host with a current density of 2.0 mA cm^{-2} and calculated the efficiency by measuring the capacity of stripped Li.

NCM 523 cathodes were prepared by mixing NCM 523 powders, Super C carbon and polyvinylidene fluoride binder at a mass ratio of 85:5:10 in N-methyl-2-pyrrolidone and coating the slurry onto Al foil. In the Li metal cell test, we pre-delithiated the NCM 523 cathode by charging it to 4.2 V at a current density of 0.5 mA cm^{-2} in a 1 M LiPF$_6$ in EC/EMC with 2% LiBOB electrolyte and paired it with Li anodes with the designed capacity. In this way, the capacity can be precisely controlled and the gassing issue caused by the NCM 523 cathode can be excluded. The electrolyte was added into the cell using a microlitre syringe (Hamilton 701 LT, 10 μl). For a Li|NCM 523 cell with a capacity of 3.4 mAh cm^{-2} and an electrode area of 1.13 cm^2, 26.9 μl electrolyte was used and the electrolyte-to-capacity ratio is correspondingly 7 μl mAh^{-1}.

Electrolyte and Li retention in practical Li metal cells. To prepare the samples for the ^{19}F qNMR test, the electrolyte was extracted from the cycled cells with 0.3 ml EMC, six times for each. The solution was then mixed with 0.2 ml deuterated dimethylsulfoxide solution of fluorobenzene (0.1 M) in an NMR tube. We followed this procedure to prepare uncycled electrolyte samples as well to reduce errors as much as possible. The electrolyte amount, corresponding to the peak area of PF$_6$ anions, was normalized to 100% by comparing with the internal reference. Owing to the constant content of the internal reference in all samples, we can use it to quantitatively measure the electrolyte retention. To test the amount of active Li left over in the cycled cells, we performed a delithiation treatment to both the NCM 523 and the 3D host, respectively, using fresh cells, and recorded the capacities. The Li retention is calculated on the basis of the amounts of leftover Li after cycling and initial Li used in the cell.

Data availability
The datasets generated during and/or analysed during the current study are available from the corresponding author on reasonable request.

References
46. Kovtyukhova, N. I. et al. Layer-by-layer assembly of ultrathin composite films from micron-sized graphite oxide sheets and polycations. *Chem. Mater.* **11**, 771–778 (1999).
47. Green, C. P. & Sader, J. E. Frequency response of cantilever beams immersed in viscous fluids near a solid surface with applications to the atomic force microscope. *J. Appl. Phys.* **98**, 114913 (2005).
48. Kuznetsov, V. et al. Wet nanoindentation of the solid electrolyte interphase on thin film Si electrodes. *ACS Appl. Mater. Interfaces* **7**, 23554–23563 (2015).
49. Greaves, G. N., Greer, A. L., Lakes, R. S. & Rouxel, T. Poisson's ratio and modern materials. *Nat. Mater.* **10**, 823–837 (2011).
50. Carpick, R. W., Ogletree, D. F. & Salmeron, M. A General equation for fitting contact area and friction vs load measurements. *J Colloid Interface Sci.* **400**, 395–400 (1999).
51. Piétrement, O. & Troyon, M. General equations describing elastic indentation depth and normal contact stiffness versus load. *J. Colloid Interface Sci.* **226**, 166–171 (2000).
52. Ebenstein, D. M. & Wahl, K. J. A comparison of JKR-based methods to analyze quasi-static and dynamic indentation force curves. *J. Colloid Interface Sci.* **298**, 652–662 (2006).